e-ISSN 2150-5551
CN 31-2103/TB

Nano-Micro Letters

ARTICLE

https://doi.org/10.1007/s40820-024-01605-z

Cite as
Nano-Micro Lett.
(2025) 17:101

Received: 3 September 2024
Accepted: 23 November 2024

$Ti_3C_2T_x$ Composite Aerogels Enable Pressure Sensors for Dialect Speech Recognition Assisted by Deep Learning

Yanan Xiao[1], He Li[1], Tianyi Gu[1], Xiaoteng Jia[1] ✉, Shixiang Sun[1], Yong Liu[1], Bin Wang[1], He Tian[2], Peng Sun[1,3], Fangmeng Liu[1,3] ✉, Geyu Lu[1,3]

HIGHLIGHTS

- Emphasized the innovation in both the material design and methodology between the sensing performance and mechanical properties.
- The composite aerogel pressure sensors exhibited low hysteresis (13.69%), wide detection range (6.25 Pa-1200 kPa), and cyclic stability to acquire stable and accurate pronunciation signals.
- Over 6888 and 4158 pronunciation signals were collected by the pressure sensor and utilized for training the convolutional neural network model, allowing for accurate recognition of six dialects (96.2% accuracy) and seven words (96.6% accuracy).

ABSTRACT Wearable pressure sensors capable of adhering comfortably to the skin hold great promise in sound detection. However, current intelligent speech assistants based on pressure sensors can only recognize standard languages, which hampers effective communication for non-standard language people. Here, we prepare an ultralight $Ti_3C_2T_x$ MXene/chitosan/polyvinylidene difluoride composite aerogel with a detection range of 6.25 Pa-1200 kPa, rapid response/recovery time, and low hysteresis (13.69%). The wearable aerogel pressure sensor can detect speech information through the throat muscle vibrations without any interference, allowing for accurate recognition of six dialects (96.2% accuracy) and seven different words (96.6% accuracy) with the assistance of convolutional neural networks. This work represents a significant step forward in silent speech recognition for human–machine interaction and physiological signal monitoring.

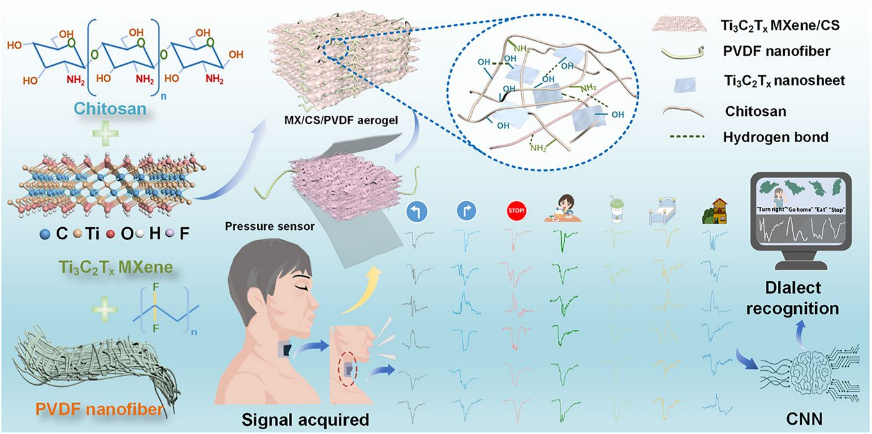

KEYWORDS Pressure sensor; Wearable sensor; $Ti_3C_2T_x$ composite aerogel; Dialect speech recognition

---

Yanan Xiao and He Li have contributed equally to this work.
✉ Xiaoteng Jia, xtjia@jlu.edu.cn; Fangmeng Liu, liufangmeng@jlu.edu.cn
[1] State Key Laboratory of Integrated Optoelectronics, College of Electronic Science and Engineering, Jilin University, Changchun 130012, People's Republic of China
[2] School of Integrated Circuits, Tsinghua University, Beijing 100084, People's Republic of China
[3] International Center of Future Science, Jilin University, Changchun 130012, People's Republic of China

1 Introduction

Spoken recognition as a branch of speech recognition can assist people with language barriers as well as human–computer interactions to express ideas and give instructions. The present spoken recognition involves the detection of sound waves directly, including spectral analysis, extraction and comparison of acoustic features, and acoustic texture analysis [1–3]. However, the direct detection approach is susceptible to interference by the transmission media, ambient noise, and the physiological state of the speakers. Speech recognition through mechanical sensors can avoid these defects by detecting the vibration of throat muscles based on the anatomical foundation of the throat during vocalization [4–7].

Wearable pressure sensors that can convert throat vibrations into visualized electrical signals have received widespread attention in detecting speech information [8–11]. Initially, speech recognition was mainly implemented by comparing the waveforms of electrical signals of throat vibrations captured using pressure sensors or tactile sensors [12, 13]. In addition, the pressure sensor can detect vibrations within the throat muscles and distinguish different pronunciations by simple signal processing, such as calculating the slope of signal peaks and comparing peak widths [14]. With the advancement of artificial intelligence (AI) technology, machine learning was introduced to build models for training and recognition of different pronunciations, particularly the combination of pressure sensors and machine learning [15–20]. Convolutional neural network (CNN) and support vector machine have frequently been introduced to identify the collected pronunciation signal for speech recognition [8, 21]. However, pressure sensors for speech recognition are currently restricted to identifying standard languages, which hampers effective communication for dialect speakers [5, 22]. For tone languages, the differences between dialect pronunciations are tone and pitch, which are generated by the throat muscles controlling the movement of the hyoid bone and cartilage. The elevation or depression of voice pitch is closely related to the contraction and relaxation of the throat muscles. The primary challenge in dialect recognition through pressure sensors with narrow-detection range and hysteresis lies in the difficulty in capturing the subtle and rapid vibrations of throat muscles during the vocalization process [23]. These factors place stringent demands on the pressure-sensing performance, such as low detection limit, high stability, and hysteresis characteristics.

To fulfill the requirements for speech recognition, $Ti_3C_2T_x$ MXene has emerged as a promising candidate for wearable pressure sensors due to its adjustable layer spacing and superior conductivity [24–26]. However, pure $Ti_3C_2T_x$ typically suffers from mechanical brittleness and oxidization, rendering it susceptible to collapse during repeated cycles [27]. To prevent sensitivity degradation under mechanical stimuli, compositing $Ti_3C_2T_x$ layers with a nanostructured polymer matrix offers enhanced specific surface area and more contact points [28]. An aerogel structure with high porosity is essential for creating efficient electrical connections and increasing the compressibility of the sensor layer [29], resulting in changes in electrical conductivity when exposed to external pressure. Chitosan (CS), as a polysaccharide biopolymer, may substantially increase the degree of freedom in molecular movement, ultimately improving flexibility by forming robust hydrogen bonding between the biopolymer and $Ti_3C_2T_x$ [30, 31]. Polyvinylidene difluoride (PVDF) short fibers, serving as a reinforcing phase, improve the durability of the aerogel by providing reversible deformation under high pressure as well [32–35]. Compared to the widely used conductive aerogel for pressure sensor, this polymer fibers reinforcement aerogel outperforms conductive aerogel by leveraging low density, excellent reversible deformation under high pressure for wide detection range, as well as low detection limit attributed to low compression modulus for the acquisition of small signals during speech recognition. Therefore, compositing polymers into $Ti_3C_2T_x$-based aerogels is a feasible approach to achieving wearable pressure sensors with enhanced sensitivity and mechanical stability.

Herein, we have fabricated wearable pressure sensors based on the laminar-like aerogel structure of $Ti_3C_2T_x$ MXene/CS/PVDF composites (Fig. 1a). A CNN algorithm is adopted to manage the sensing information acquired by pressure sensors, leading to accurate dialect recognition (96.2% for six dialects and 96.6% for seven common vocabularies) that can satisfy the communication demand for dialect-speaking people (Fig. 1b). This work propels the development of pressure sensors for dialect recognition.

https://doi.org/10.1007/s40820-024-01605-z

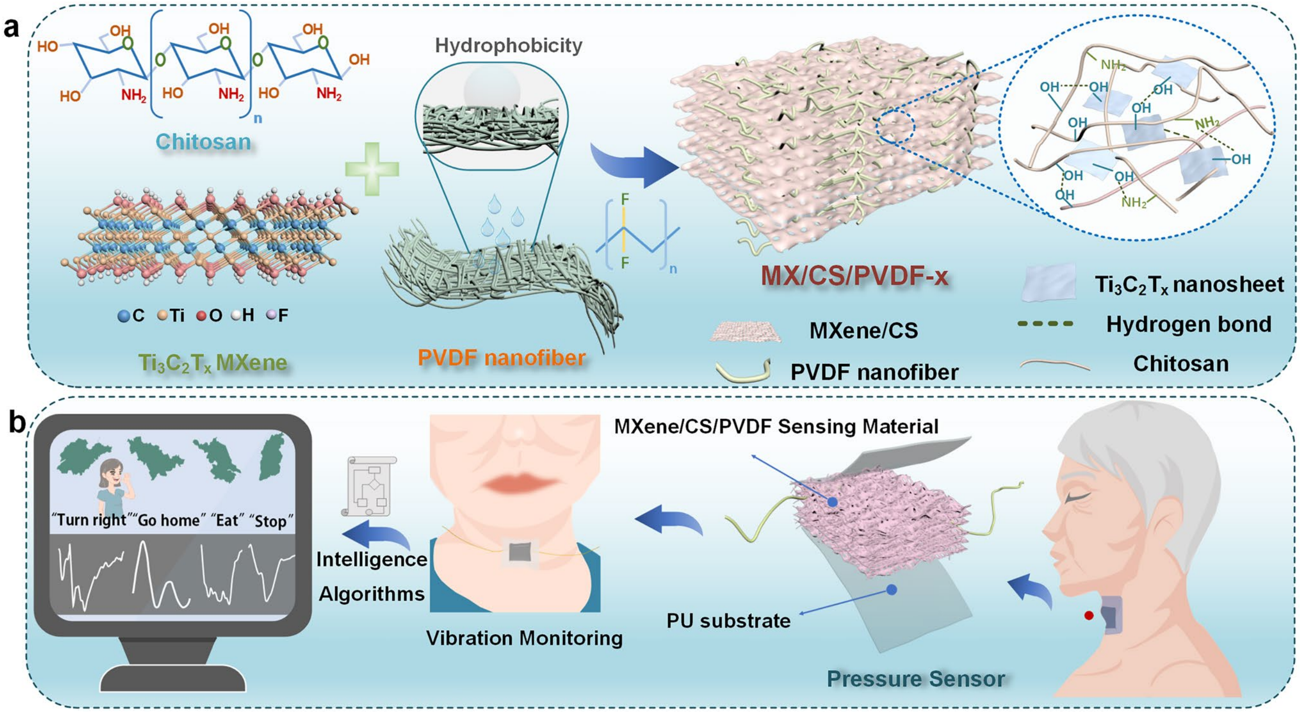

Fig. 1 **a** Schematic preparation of MX/CS/PVDF aerogel. **b** Wearable Ti$_3$C$_2$T$_x$-based aerogel pressure sensor for dialect speech recognition

2 Experimental

2.1 Preparation of Ti$_3$C$_2$T$_x$ MXene Nanosheet

Ti$_3$C$_2$T$_x$ MXene nanosheets were synthesized by less violently etching the Ti$_3$AlC$_2$ (Jilin 11 Technology Co., Ltd., China) utilizing LiF/HCl mixed solution for removing the Al layer from the MAX phase. First, 2 g LiF (Aladdin, > 99.99%) was slowly dissolved in 80 mL 12 M HCl (Xilong Scientific Co., Ltd.) in a Teflon lining with vigorous stirring for 15 min at room temperature. 2 g Ti$_3$AlC$_2$ was then gradually added into the above mixed solution and reacted at 45 °C of water bath for 24 h. After etching, the resultant mixture was repeatedly centrifuged for 8 min at 8000 rpm until the pH of the supernatant reached 6 ~ 7. The clay mixture was ultrasonically dispersed in an ice bath at 350 W for 1 h. Finally, Ti$_3$C$_2$T$_x$ MXene nanosheets were obtained by centrifugation at 10,000 rpm for 10 min.

2.2 Preparation of PVDF Fibrous Membrane

PVDF fibrous membranes were prepared by solution electrospinning. The electrospinning precursor solution was 8 wt% PVDF (Solef 6010, Solvay S.A) in DMF and acetone mixture (7/3, w/w) and placed in 10 mL syringes with a 19 g blunt needle and controlled by programmed syringe pumps with 0.8 mL h^{-1} feed rate. 16 kV high voltage was provided by a high voltage power supply with a nozzle-to-collector distance of 18 cm. In the electrospinning process, the environment humidity and temperature were fixed at 58 ± 2%, 20 °C.

2.3 Preparation of MX/CS/PVDF Aerogels

0.5 g above PVDF fibrous membrane was put into 500 mL deionized water and broken into suspension by a high-speed blender for 10 min. Then, 2.5 g CS (Aladdin, degree of deacetylation ≥ 75%) and 5 mL acetic acid (Xilong Scientific Co., Ltd., > 99.5%) were dissolved in the above mixture. After stirring for 20 min, the different weight of Ti$_3$C$_2$T$_x$ MXene nanosheet was added into CS/PVDF suspension, and the weight ratios of Ti$_3$C$_2$T$_x$ and CS were 0.5/1, 1/1, 1.5/1, 2/1, respectively.

Homogeneous aerogel precursor solutions were obtained by ultrasound treatment for 20 min. Then, 8 mL aerogel precursor was injected into 4 × 4 × 4 cm^3 Teflon mold and was directly frozen from the bottom by liquid nitrogen. Subsequently, the mixture was freeze-dried in a vacuum lyophilizer (Beijing Biocool Co., Ltd., FD-1A-50) for 16 h. Herein, the sample was defined as MX/CS/PVDF-x ($x = 0.5$, 1, 1.5, 2), where x was represented as the ratio between $Ti_3C_2T_x$ MXene and CS.

2.4 Characterizations

The morphology of $Ti_3C_2T_x$ MXene nanosheet, PVDF fibrous membrane, and MX/CS/PVDF-x ($x = 0.5$, 1, 1.5, 2) was observed by scanning electron microscopes (SEM, Hitachi TM4000Plus and FESEM, JEOL JSM-7900F) with an acceleration voltage of 5 kV. The morphology of $Ti_3C_2T_x$ MXene was observed by transmission electron microscopy (TEM; JEM 2100 F) with an acceleration voltage of 200 kV. The surface properties were determined by an atomic force microscope (AFM, CSPM5500). The chemical components and structure over a range of 4000–400 cm^{-1} were measured by a Fourier-transform infrared spectroscopy spectrometer (FTIR, Nicolet iS10). The crystalline structures were characterized by wide-angle X-ray diffraction (XRD, Rigaku D/Max 2550) in the 2θ range from 3° to 50° with Cu Kα radiation ($\lambda = 1.5418$ Å). The scanning rate was 5° min^{-1}. The chemical composition of the $Ti_3C_2T_x$-based aerogel surfaces was examined by X-ray photoelectron spectroscopy (XPS, ESCALAB 250) with an X-ray source (Al Kα hυ = 1486.6 eV). The Raman spectra from 100 to 2000 cm^{-1} were analyzed using a 632 nm laser by a Raman confocal micro-spectrometer (LabRAM HR Evolution, Horiba, France). The specific surface area and pore size distribution were measured by nitrogen adsorption/desorption isotherms through Brunauer–Emmett–Teller (BET, Autosorb-iQ-C).

Pressure-sensing performances: The different pressure conditions were achieved by a digital force gauge (M5-5, Mark10), electrodynamic measuring table (ESM303, Mark10) and compression testing machine with TRAPEZIUM X pressure acquired software (AGS-X 500 N, Shimadzu, Japan). The real-time current change of the sensor was measured by connecting the digital multimeter (Keithley DMM7510) with 0.1 V DC voltage provided by a DC power supply (DPS-305BM). The response (R_I) was defined as relative current change ($\Delta I/I_0$), where ΔI represents the change of the current between the loading pressure state and the initial state. Additionally, the sensitivity (S) of the pressure sensor was defined as $\delta R_I/\Delta p$, where p refers to the intensity of pressure. The electrical hysteresis was defined as ratio of the area beneath $\Delta I/I_0$ curves under loading and unloading.

$$Hysteresis(\%) = \frac{S_{\text{unloading}} - S_{\text{loading}}}{S_{\text{loading}}} \times 100\% \quad (1)$$

where S_{loading} and $S_{\text{unloading}}$ represent the integral area of the $\Delta I/I_0$ and pressure curves under pressure loading and unloading, respectively.

2.5 Finite Element Simulation of the Stress Distribution

The COMSOL Multiphysics software was utilized to conduct the finite element (FE) simulation. For simulating the stress distribution, the "Solid mechanics" module, coupled with the "Stationary" study, was employed. First, we build the geometric model of the pressure sensor. The laminated aerogel was set to be six rectangles with 4 mm width and 0.005 mm height, and the applied force was distributed on a semicircle given a non-deformable metal material with a radius of 1 mm. Moreover, six contact pair nodes were set between the stress loaded object and the aerogel top surface layer, the aerogel lamellae, respectively. Subsequently, the left and right boundaries of the aerogel lamellae were set as fixed constraint node and the mesh was constructed on the models by Free Triangular feature node. Ultimately, the computation was executed to acquire the distribution of the stress for aerogel when subjected to different pressures.

3 Results and Discussion

3.1 Preparation and Characterization of MX/CS/PVDF Aerogels

The fabrication process of $Ti_3C_2T_x$ MXene/CS/PVDF (MX/CS/PVDF) composites aerogels is displayed in Fig. S1. The monolithic $Ti_3C_2T_x$ (lattice stripe spacing: ~ 0.251 nm, Fig. S2), CS, and PVDF fibers (Fig. S3a) suspension were mixed uniformly followed by freeze-drying to yield an aerogel (Fig. S3b). SEM images of the interconnected and lamellar-structure aerogel (Fig. 2a) revealed the evolution of MX/CS/PVDF-x aerogel morphology with increased $Ti_3C_2T_x$ concentrations.

https://doi.org/10.1007/s40820-024-01605-z

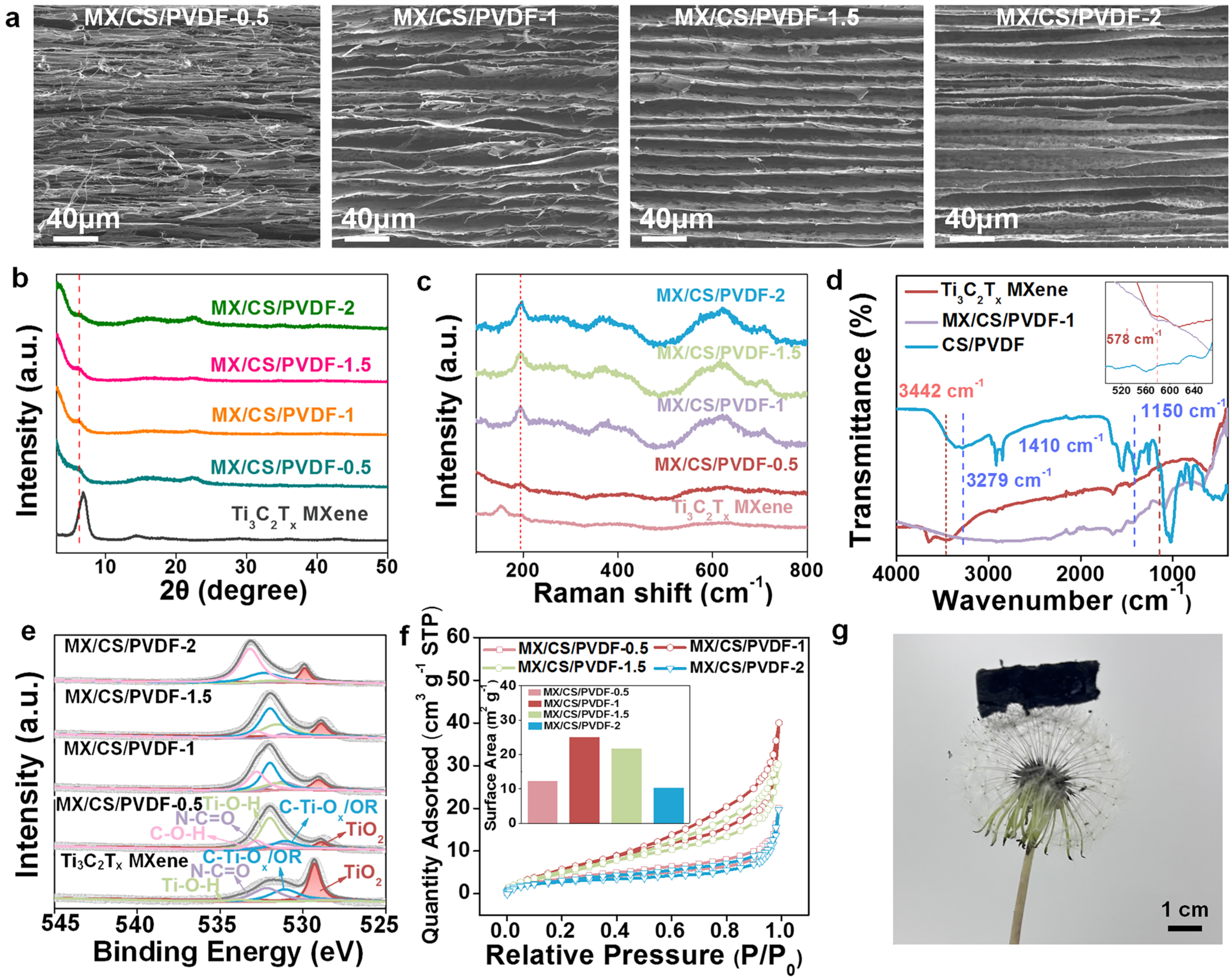

Fig. 2 Characterization of MX/CS/PVDF aerogels. **a** SEM images of the cross-section morphologies. **b** XRD patterns and **c** Raman spectra of $Ti_3C_2T_x$ nanosheet and MX/CS/PVDF aerogels. **d** FTIR spectra of $Ti_3C_2T_x$ nanosheet, CS/PVDF, and MX/CS/PVDF-1 aerogel. **e** O 1*s* XPS spectra of $Ti_3C_2T_x$ nanosheet, MX/CS/PVDF aerogels. **f** N_2 adsorption–desorption isotherms of MX/CS/PVDF aerogels. **g** Photograph of an ultra-lightweight aerogel cut into 2 × 2 cm^2 pieces placed on the taraxacum mongolicum

MX/CS/PVDF-0.5 showed a tighter structure with less space between the lamellae. The space became wider and the structure evolved more loosely in MX/CS/PVDF-1. However, higher $Ti_3C_2T_x$ content resulted in the congregating and compact structure of the aerogel, because of the strong intermolecular forces between $Ti_3C_2T_x$ nanosheets. SEM and elemental mapping images of MX/CS/PVDF lamellae indicated that $Ti_3C_2T_x$ were evenly distributed in aerogel due to the strong hydrogen bond between CS and $Ti_3C_2T_x$. The PVDF short fibers were randomly distributed within the aerogel, locating between the layers of the aerogel sheet, embedded within the aerogel lamellae, and on the surface of the aerogel lamellae (Figs. S4-S6). The AFM images proved the evolution of aerogel surface roughness and morphology with increased $Ti_3C_2T_x$ concentrations (Fig. S7).

The structure of MX/CS/PVDF aerogels was characterized by XRD, Raman, FTIR, and XPS. The XRD pattern showed that the (002) peak shifted toward the low-angle direction and a decrease in intensity, indicating expanded layer spacing of the $Ti_3C_2T_x$ layer caused by the addition of CS and PVDF nanofibers (Figs. 2b and S8). The A_{1g}, relevant to the out-of-plane vibration of Ti and C atoms, shifted from 151 to 194 cm^{-1} and the cell surface unit deformed in Confocal Raman spectroscopy (Fig. 2c) [36]. The robust hydrogen bonding between CS and $Ti_3C_2T_x$ was confirmed

Table 1 Comparison of the density and maximum stress between the prepared conductive aerogel in this article and previous articles

Density (mg cm^{-3})	Maximum stress (kPa)	Material	References
66.3	~89.4 (100 cycles)	MXene@carboxylated carbon tube/carboxymethyl chitosan	[57]
10.3	~58	Polyimide/carbon tube	[58]
25	~49.8	MXene/aramid nanofibers	[59]
10	~1.2	Polysiloxane cross-linked MXene	[60]
50	~40	Sodium alginate/MXene/polydimethylsiloxane	[61]
17		Graphene oxide/dopamine/polyaniline	[62]
7–20.7	~30	MXene/chitosan	[63]
14.67		Polypyrrole/cellulose acetate	[64]
13.3	~30	Alkali lignin/carbon nanofiber	[65]
11.2		Poly(3,4-ethylenedioxythiophene):polystyrene sulfonic acid/carbon nanofiber	[66]
6.7		Carbon nanofiber-Graphene oxide/glucose-kaolin carbon	[67]
25.6	~22.5 (3000 cycles)	R-graphene oxide/polyimide	[68]
8.16	~75 (300 cycles)	Graphene oxide/hydroxypropyl methyl cellulose	[69]
20.54	~800 (100 cycles)	Polyacrylonitrile nanofibers/polyvinyl alcohol/carbon tube/hydrophobic octadecylamine functionalized r-graphene oxide	[70]
12.6–26.5		FeS_2/carbon tube	[71]
7.48	~6 (100 cycles)	Carbon nanofiber/carbon tube/MXene	[72]
12		AgNWAs/carboxymethyl cellulose	[73]
42.7	~50	Chitosan/carbon tube	[74]
260		MXene/carbon nanofiber/thermoplastic urethane	[75]
200–300		Carbon tube	[76]
228	~800 (1000 cycles)	Graphene armor	[77]
6.86	~108 (100 cycles)/1769.5 (1 cycle)	$Ti_3C_2T_x$ MXene/chitosan/polyvinylidene difluoride	This work

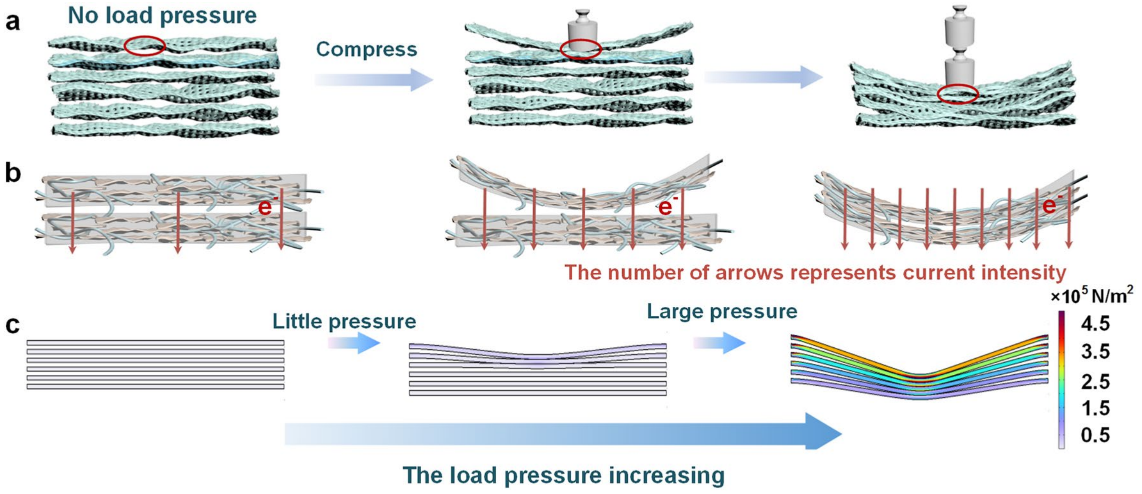

Fig. 3 Piezoresistive effect of MX/CS/PVDF aerogel pressure sensor. **a** Schematic of the pressure sensor under different load pressures. **b** Illustration of MX/CS/PVDF lamellae deformation states and the electron transport process under different pressures. **c** Compressing deformation mechanism of MX/CS/PVDF-1 pressure sensor explained by FE simulation. The color contours represent the microscopic strain of the aerogel structure during the deformation process

https://doi.org/10.1007/s40820-024-01605-z

by broadening and blue shift of peaks around 2240 cm^{-1} of MX/CS/PVDF-1 compared to $Ti_3C_2T_x$ and CS/PVDF aerogel (Fig. 2d) [37]. Moreover, the vibration peaks of Ti–O, -NH, -CF_2, and β phase could be observed in the FTIR spectra, indicating the successful preparation of MX/CS/PVDF aerogel [38]. The chemical states and bonding configurations were revealed by XPS patterns (Fig. 2e). The O 1*s* peak showed that the oxidation of $Ti_3C_2T_x$ was retard as a result of the formation of hydrogen bonds between $Ti_3C_2T_x$, CS, and PVDF. The involvement of CS and PVDF reduced the peak area of the TiO_2 phase. However, an excessive amount of $Ti_3C_2T_x$ increased the oxidation process due to the exposure of susceptible oxidation groups [39].

The MX/CS/PVDF-x aerogel had a high specific surface area of 25.025 m^2 g^{-1} (Fig. 2f inset) and ultralow density ($\rho < 6.86$ mg cm^{-3}) of MX/CS/PVDF-1, which could be placed on the surface of the taraxacum mongolicum without deformation (Fig. 2g). The N_2 adsorption/desorption isotherms of MX/CS/PVDF-x exhibited a representative H3 hysteresis loop and II isotherms (Fig. 2f), indicating that the adsorption of $Ti_3C_2T_x$-based aerogel occurred as a multilayer reversible adsorption process on the surface of mesoporous or macroporous [40–42]. Moreover, the inflection point was located near the monolayer adsorption and the multilayer absorption was developed with P/P_0 increasing. The limit equilibrium adsorption value cannot be observed from the isotherm due to the endless absorption layers.

The stable mechanical properties of MX/CS/PVDF were demonstrated by repeated compression–relaxation tests (Fig. S9a-c). Compared with $Ti_3C_2T_x$ MXene/CS aerogel (Fig. S9d-f), the MX/CS/PVDF aerogel exhibited elasticity that could fully recover to the original state as the load pressure (35.39 -1769.5 kPa) was removed. The durability of MX/CS/PVDF-1 revealed almost no attenuation of the ultimate stress during 100 cycles of repeated compression–relaxation. In contrast to $Ti_3C_2T_x$ MXene/CS, the addition of PVDF short fibers served as reinforced phase remarkably enhanced the durability and mechanical stability of aerogel. When suffering high pressure, the reinforced phase buffered and dispersed most of the stresses, prevented irreversible deformation and prevented damage to the conductive pathways of the substrate materials. The MX/CS/PVDF aerogel exhibited extraordinary performances such as lightweight and mechanical properties compared with conductive aerogel in previous work (Table 1).

3.2 Pressure-Sensing Performance

The pressure sensor was fabricated by fixing the copper wires as electrodes on the top and bottom surfaces of the MX/CS/PVDF aerogel and then simply encapsulated with waterproof and flexible polyurethane (PU) with 14 µm thickness (Fig. S10). The effect of the encapsulation layer thickness and sensitive materials thickness on the sensing performance was investigated in Supporting Information (Figs. S11-S14). Figure 3a demonstrates the strain behavior where the top thin lamellae of MX/CS/PVDF were bent and deformed under ultralow applied pressure, while the inner $Ti_3C_2T_x$ nanosheets become closer. When the load pressure increased, the top thin lamellae and the bottom of MX/CS/PVDF underwent deformations. Therefore, the conductive pathway of MX/CS/PVDF aerogel increased with an accelerated electron transport rate, resulting in a larger relative current (Fig. 3b). The sharp increase in conductive pathways was contributed by the deformations of $Ti_3C_2T_x$-based lamellae and the increase in contact area of MX/CS/PVDF lamellae. As the load pressure continued to increase, MX/CS/PVDF lamellae stopped deforming. The contact area between the lamellae expanded until full contact was established and conducting pathways were no longer increased, while the electron transport rate reached maximum.

To illustrate the working mechanism of the MX/CS/PVDF aerogel-based pressure sensor, finite element simulations were conducted to calculate the stress distribution during the loading process (Fig. 3c). By applying a small load pressure, the stress was distributed throughout the top aerogel lamellae, causing a fraction of the aerogel to deform when it came into contact with one another. The stress distribution range and the contact area between the aerogel lamellae both grew with increasing load pressure. This process of change aligned with the actual situation.

The sensing performances of MX/CS/PVDF aerogel were measured under various levels of pressure. MX/CS/PVDF-1 exhibited the highest sensitivity in the pressure range of 0–1200 kPa (Fig. 4a). The mechanism was that the sensitivity of the pressure sensor was primarily associated with the number of conductive pathways inside the aerogel before and after pressure loading and unloading, and the number of conductive pathways of the MX/CS/PVDF-x sensor was determined by the content of $Ti_3C_2T_x$ nanosheets and specific surface area. Owing to low $Ti_3C_2T_x$ content

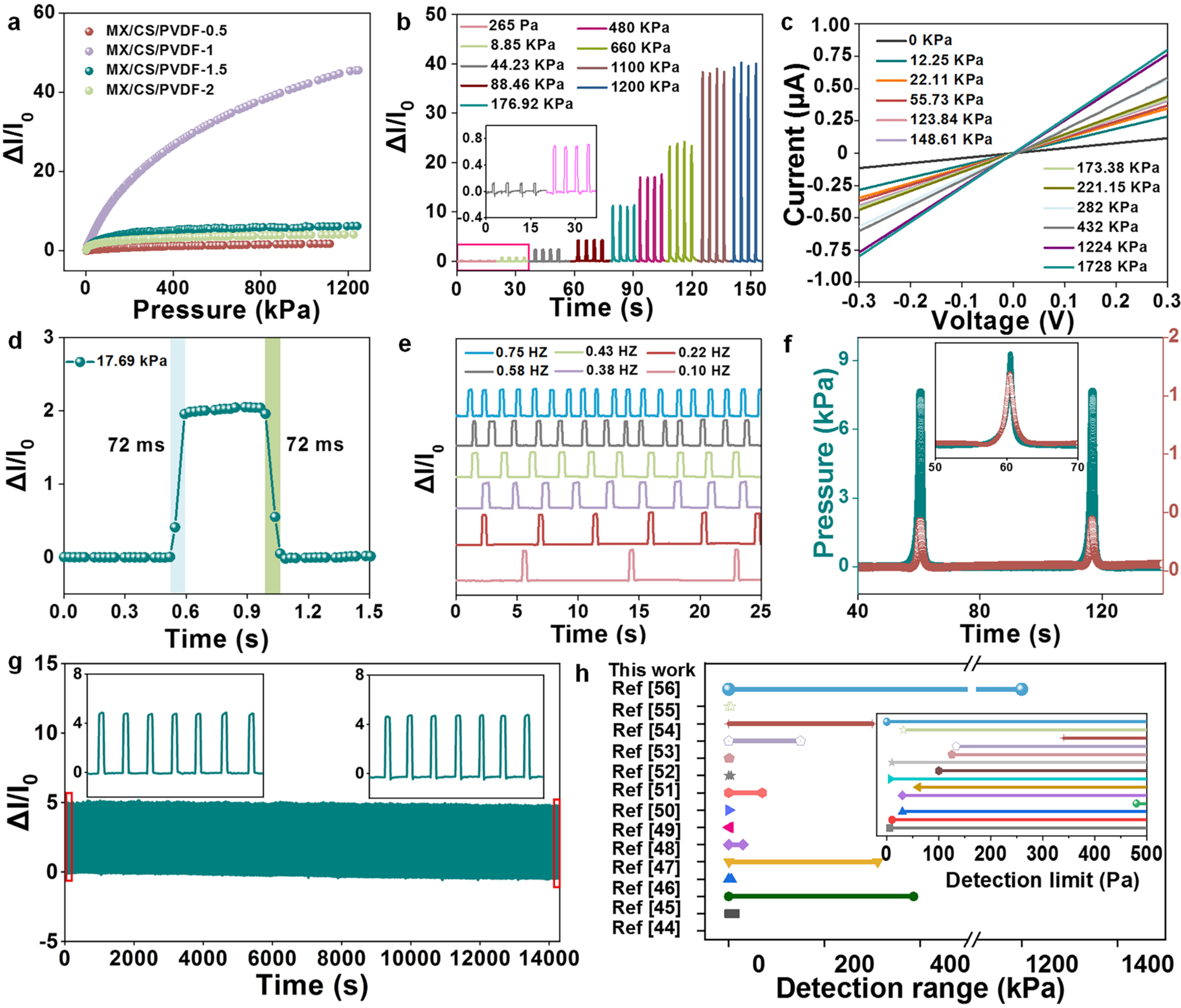

Fig. 4 Pressure-sensing performances of MX/CS/PVDF-1 aerogel pressure sensor. **a** Response-pressure curves of MX/CS/PVDF with different $Ti_3C_2T_x$ concentrations. **b** Relative current changes under load pressure of 265 Pa-1200 kPa. **c** The I-V curves of the MX/CS/PVDF-1 sensor under different load pressures. **d** Response and recovery time at a pressure of 17.69 kPa. **e** The variation of I-t curves with different running frequencies load pressure. **f** Instantaneous response of I-t and P–t curves. **g** Durability test under 6000 loading/unloading cycles at a pressure of 22.12 kPa, inset shows the enlarged curve for the first seven cycles and last seven cycles. **h** Performance comparison of piezoresistive sensors

and specific surface area, a sufficient number of conductive pathways could not be established inside MX/CS/PVDF-0.5 aerogel, and the conductive pathways did not change much even after loading pressure (Fig. S15a). For MX/CS/PVDF-1.5 and MX/CS/PVDF-2, due to the excessively high $Ti_3C_2T_x$ content and the reduced specific surface area, sufficient conductive pathways were already established within the aerogel without pressure loading being received, so that the number of conductive pathways did not change much when pressure loading was applied (Fig. S15c, d).

With load pressure continuously increasing from 265 Pa to 1200 kPa, the relative current intensity gradually increased, allowing for effectively distinguishing different levels of load pressure (Figs. 4b and S16). The sensitivity ratio for MX/CS/PVDF-1 was 0.11 kPa^{-1} in the range of 0–106 kPa (Fig. S15b). As applied pressure increased from 106 to 400 kPa, the sensitivity decreased to 0.055 kPa^{-1}, and when the pressure was higher than 400 kPa, the sensitivity was decreased to 0.022 kPa^{-1}. Therefore, the sensing performance of MX/CS/PVDF-1 with the optimal output signal would be explored under different input load

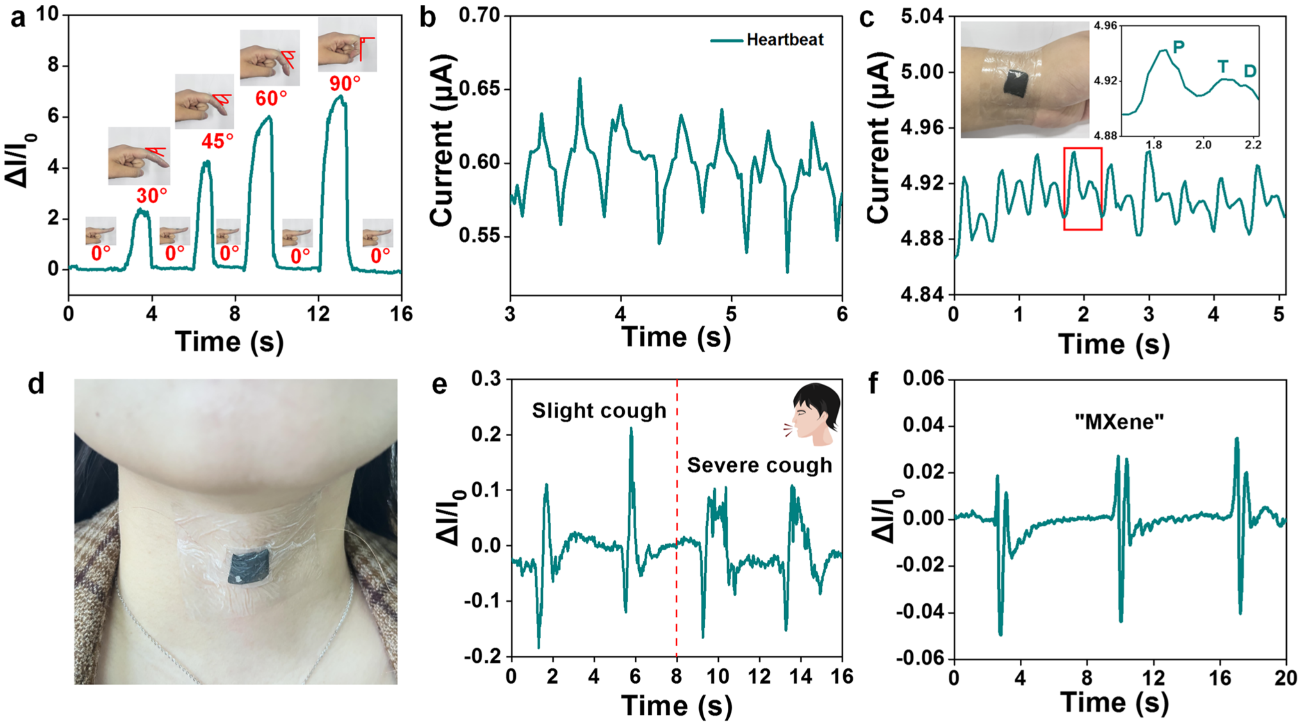

Fig. 5 Real-time monitoring of human physiological signals using the piezoresistive sensor. **a** Relative current change of finger bending angle from 0 to 30, 45, 60, 90 degrees. **b** Real-time recording of the heartbeat waveform. **c** Real-time recording of the wrist pulse waveform (The inset illustrates the enlarged view of the pulse vibration waveform). **d** Detection of human physiological signals when the MX/CS/PVDF-1 was fixed on the throat of a 24-years-old volunteer: **e** Cough, and **f** Say "MXene"

pressures. Figure 4c illustrates the excellent linear relation of the current–voltage (*I-V*) curves from -0.3 to 0.3 V under various load pressures from 0 to 1728 kPa. It indicated that the ohmic contacts were formed between the MX/CS/PVDF-1 sensing layer and Cu electrodes [43]. Notably, as the load pressure increased, the slope of the *I-V* curves became steepen, indicating a decrease in device resistance and a subsequent rise in current.

This MX/CS/PVDF-1-based pressure sensor exhibited a rapid response/recovery time of 72 ms under 17.69 kPa load pressure (Fig. 4d). MX/CS/PVDF-1 emerged with extraordinary stability and distinguishable response signal at different frequencies from 0.1 to 0.75 Hz (Fig. 4e), from 0.54 Hz to 1.96 and 2.47 Hz (Fig. S17). The low hysteresis of 13.69% is demonstrated in Fig. S18 and further confirmed by the output current change signal and the consistency of the input load pressure and current signals during pressure loading and unloading (Fig. 4f). Additionally, little attenuation and a nearly identical relative current change were observed during 6000 cycle tests at 22.12 kPa pressure. The identical current amplitude of the initial and end states proved the durability (Fig. 4g). The long-term stability of the MX/CS/PVDF-1 pressure sensor was confirmed by the consistency of the initial current and the relative current change under 15.91 kPa over a period of one month (Fig. S19). The initial current was stable for 31 days and the relative current response to pressure had no significant attenuation. MX/CS/PVDF-1 pressure sensors demonstrated superior stability under varying ambient humidity and temperature, and it was discussed extensively in Supporting Information (Fig. S20).

The pressure sensor can detect a low load pressure of 6.25 Pa (Fig. S21). It attributed to an ultralow compression modulus of 0.234 kPa of MX/CS/PVDF-1 that deformed under ultralow load stress and generated visual electrical signals (Fig. S12a). There was a factor responsible for this instance that the elongated chain structure was formed in aerogel by hydrogen bonding between chitosan and $Ti_3C_2T_x$ for the increased freedom degree of molecular movement. Moreover, the pressure sensor demonstrated a revisable deformation under high pressure due to the introduction of PVDF short fibers which ensured the reversible output response signals under wide detection range (Fig. S22a-c).

Taken together, the detection ranges of the MX/CS/PVDF-1 outperformed previously reported aerogel-based pressure sensors, with a low detection limit of 6.25 Pa, maximum detection range of 1200 kPa, and excellent stability (Fig. 4h) [44–56]. The effect of PVDF fibers length and the laminated structure or random structure on the sensing performance was further investigated in Supporting Information (Figs. S22-S24).

To further evaluate the practical feasibility, a MX/CS/PVDF-1 pressure sensor was placed on the joints and vocal cords of the human body to detect human physiological signals. It was observed that the action and physiological state of the human body could be distinguished by comparing the output signal shape and intensity of the curves in Fig. 5. The pressure sensor can effectively distinguish items weighing from 100 mg (22.6 Pa) to 20 g (1.48 kPa) and bending angles in the range from 0° to 90° (Figs. S25a and 5a). The output signal intensity varied significantly when the volunteers pressed manually between the relative low-pressure range and high-pressure range (Fig. S25b). The heartbeat and the pulse, as an important physiological signals of the human body, was detected by attaching to the chest and wrist of a 24-year-old volunteer (Fig. 5b, c). The periodic and stable wrist pulse with a regular beating

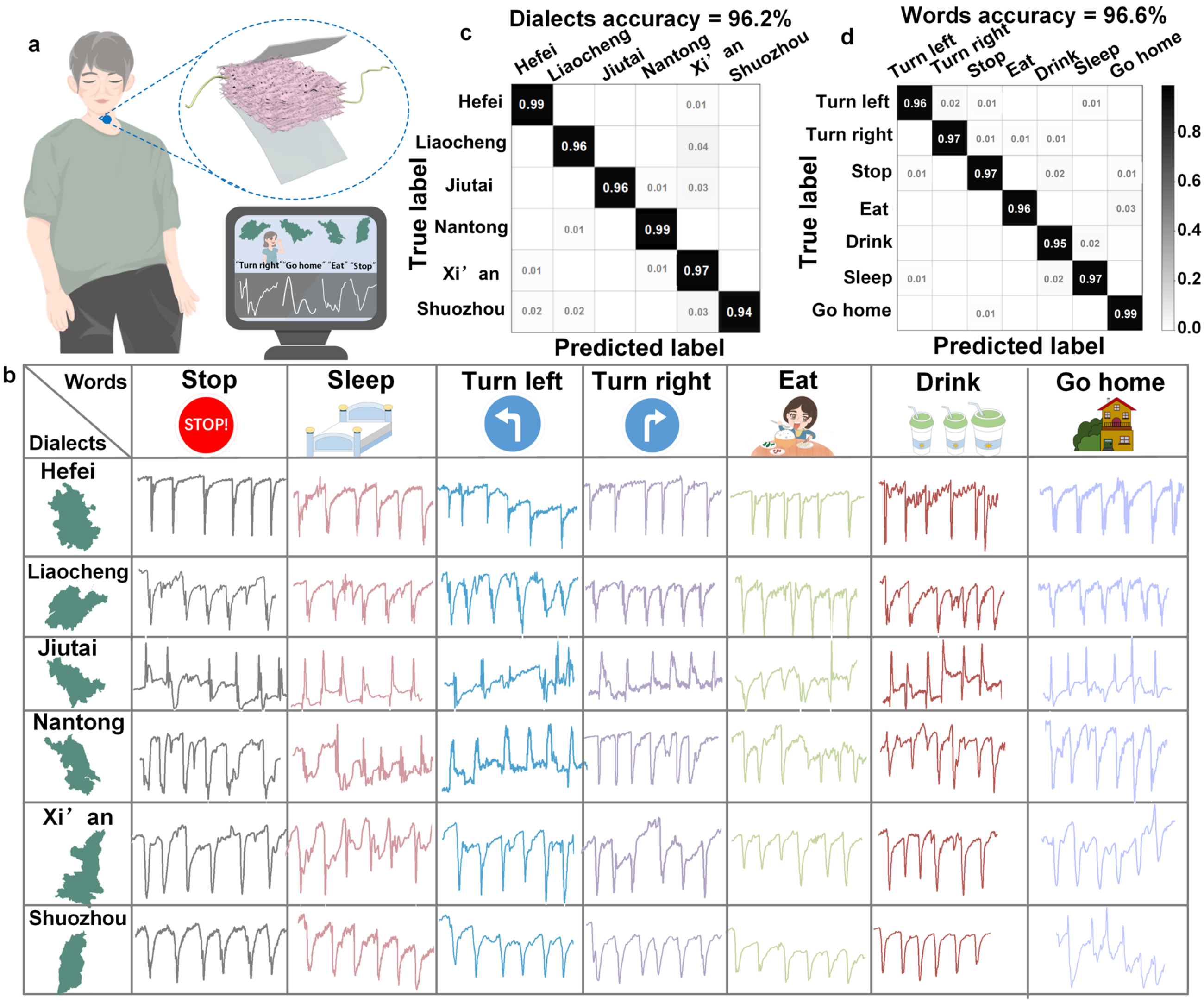

Fig. 6 Dialect speech recognition assisted by deep learning. **a** Pressure sensor was fixed on the throat for speech recognition. **b** Continuous current signal images generated by seven vocabularies in six Chinese dialects. **c** Confusion matrix of the CNN algorithm for six different Chinese dialects. **d** Confusion matrix of the CNN algorithm for seven words in different Chinese dialects

https://doi.org/10.1007/s40820-024-01605-z

of 108 beats per minute was illustrated, where three faint characteristic peaks percussion wave (P), tidal wave (T), and diastolic wave (D) of the human pulse could be clearly distinguished (Fig. 5c). Furthermore, human actions including swallowing, yawning, and coughing could be precisely detected when the sensor was placed on the throat (Figs. 5c, e, and S25c, d). Meanwhile, it can accurately capture the throat vibration during human pronunciation, which showed significant differences in waveforms of “Wearable,” “Sensor,” and “MXene” (Fig. 5f and S25e, f).

3.3 Dialect Speech Recognition Based on MX/CS/PVDF-1 Pressure Sensor

For non-standard language people, it is extremely complicated to communicate with the natives using standard language when they need to hospitalize out-of-town or migrant work. The same dialect shares similar spoken speed, syllables, and pitches, and therefore, generates specific electrical signal waveforms, which can be effectively distinguished between dialects. When saying the same word in different dialects, there are similarities in both syllables and pronunciation patterns for the same language (Fig. S26). The MX/CS/PVDF-1-based pressure sensor demonstrated low detection limit (6.25 Pa), wide detection range (~ 1200 kPa), and low hysteresis (13.69%) that superior the previous pressure sensor for speech recognition and could acquire stable signals (Table S1).

To satisfy the demand for dialect speech recognition, the MX/CS/PVDF-1 based pressure sensor was fixed on the throat of six dialect speakers from Nantong, Liaocheng, Jiutai, Shuozhou, Xi’an, and Hefei. The selected dialects were representative and were primarily associated with geographic distribution from each of the six provinces in the eastern, northern, central, western, and southern parts of mainland China. To further improve the accuracy of identification, the dialects with similar pronunciation such as Hefei and Nantong dialects belonging to the Mandarin of Jianghuai, Shuozhou, and Xi’an dialects belonging to the Central Plains Mandarin were selected. Moreover, the sensing signals were obtained for further training and recognition when the dialect speakers spoke seven daily instructional words such as “stop,” “sleep,” “turn left,” “turn right,” “eat,” “drink,” and “go home.” Deep learning algorithms are employed for dialect speech recognition to achieve precise categorization and dialect recognition (Fig. 6a). Convolutional neural networks (CNNs), a translation invariant classification algorithm based on sophisticated mathematical theory, are widely utilized to mimic the cognitive learning ability of the human brain for image processing and categorization. Here, we developed a CNN algorithm with an 11-layer network for accurate classification of dialect types and the common vocabulary in the different dialects (Fig. S27). Over 6888 and 4158 vocalization vibration signals on the throat were collected by the sensor for training a CNN model to identify 7 vocabularies and 6 Chinese dialects, respectively (Fig. 6b).

The filtered processed electric signals are presented to the input layer and then perform feature extraction across four convolutional layers. The model can be partitioned into four parts, and each portion contains at least one convolutional layer and one maximum pooling layer (MP). The effect of MP is to simplify the complexity, compress the eigenvalues, and reduce the computational effort. Additionally, the convolutional layer is followed by a batch normalization layer for reducing the covariance drift in the model and improving the stability of the model. Three fully connected layers utilized for the final prediction follow the four parts. It should be noted that the dropout layer in the fully connected layer serves to reduce overfitting by ignoring half of the hidden nodes. The activation function used after MP is the ReLU.

The deep learning model based on the CNN algorithm was split into two processes. The first process was model training, where the image size was set as 64 × 64 and the batch size was 512. The loss value started to converge after 6 epochs, and the accuracy of the training set reached 100% after 16 loss values. Eventually, the accuracy of the test set reached 96.2% and 96.6% for six Chinese dialects and seven words in different dialects (Fig. 6c, d).

4 Conclusion

Here, we have fabricated MX/CS/PVDF-based pressure sensors with ultralight density and remarkable durability for dialect recognition. The elaborately designed MX/CS/PVDF-1-based pressure sensor exhibited rapid response/recovery time (< 72 ms) and a low detection limit (6.25 Pa), allowing for the detection of slight vibrations in the throat. During the process of dialectal speech recognition, over 6888 and 4158 vocalization vibration signals on the throat were obtained by saying 7 vocabularies and 6 Chinese dialects for training a CNN model. The recognition accuracy of dialect pronunciation information was 96.6% and 96.2%, respectively. This high-performance pressure sensor can have a significant role in human–machine interaction and health monitoring in the future to express instructions and acquire physiological information.

Acknowledgements This work is supported by the National Nature Science Foundation of China (No. 62122030, 62333008, 62371205, 52103208), National Key Research and Development Program of China (No. 2021YFB3201300), Application and Basic Research of Jilin Province (20130102010 JC), Fundamental Research Funds for the Central Universities, Jilin Provincial Science and Technology Development Program (20230101072JC).

Author Contributions Yanan Xiao contributed to conceptualization, methodology, data curation, and original draft writing. He Li was involved in methodology and data curation. Tianyi Gu contributed to data curation. Xiaoteng Jia was involved in conceptualization, supervision, and writing—review and editing. Shixiang Sun contributed to data curation. Yong Liu was involved in data curation. Bin Wang contributed to data curation. He Tian was involved in writing—review and editing. Peng Sun contributed to writing—review and editing. Fangmeng Liu was involved in funding acquisition, conceptualization, writing—review and editing, and supervision. Geyu Lu contributed to funding acquisition and supervision.

Declarations

Conflict of Interest The authors declare no interest conflict. They have no known competing financial interests or personal relationships that could have appeared to influence the work reported in this paper.

Supplementary Information The online version contains supplementary material available at https://doi.org/10.1007/s40820-024-01605-z.

References

1. R.V. Shannon, F.G. Zeng, V. Kamath, J. Wygonski, M. Ekelid, Speech recognition with primarily temporal cues. Science **270**, 303–304 (1995). https://doi.org/10.1126/science.270.5234.303
2. S.M.N. Woolley, T.E. Fremouw, A. Hsu, F.E. Theunissen, Tuning for spectro-temporal modulations as a mechanism for auditory discrimination of natural sounds. Nat. Neurosci. **8**, 1371–1379 (2005). https://doi.org/10.1038/nn1536
3. J. Makhoul, R. Schwartz, State of the art in continuous speech recognition. Proc. Natl. Acad. Sci. U.S.A. **92**, 9956–9963 (1995). https://doi.org/10.1073/pnas.92.22.9956
4. A. Löfqvist, T. Baer, N.S. McGarr, R.S. Story, The cricothyroid muscle in voicing control. J. Acoust. Soc. Am. **85**, 1314–1321 (1989). https://doi.org/10.1121/1.397462
5. Q. Yang, W. Jin, Q. Zhang, Y. Wei, Z. Guo et al., Mixed-modality speech recognition and interaction using a wearable artificial throat. Nat. Mach. Intell. **5**, 169–180 (2023). https://doi.org/10.1038/s42256-023-00616-6
6. D. Ravenscroft, I. Prattis, T. Kandukuri, Y.A. Samad, L.G. Occhipinti, A wearable graphene strain gauge sensor with haptic feedback for silent communications. 2021 IEEE International Conference on Flexible and Printable Sensors and Systems (FLEPS). June 20–23, 2021, Manchester, United Kingdom. IEEE, (2021). pp. 1–4.
7. T.S. Le Dinh, J. An, Y. Huang, Q. Vo, J. Boonruangkan et al., Ultrasensitive anti-interference voice recognition by bio-inspired skin-attachable self-cleaning acoustic sensors. ACS Nano **13**, 13293–13303 (2019). https://doi.org/10.1021/acsnano.9b06354
8. T. Kim, Y. Shin, K. Kang, K. Kim, G. Kim et al., Ultrathin crystalline-silicon-based strain gauges with deep learning algorithms for silent speech interfaces. Nat. Commun. **13**, 5815 (2022). https://doi.org/10.1038/s41467-022-33457-9
9. Z. Zhou, K. Chen, X. Li, S. Zhang, Y. Wu et al., Sign-to-speech translation using machine-learning-assisted stretchable sensor arrays. Nat. Electron. **3**, 571–578 (2020). https://doi.org/10.1038/s41928-020-0428-6
10. G. Ge, Y. Zhang, J. Shao, W. Wang, W. Si et al., Stretchable, transparent, and self-patterned hydrogel-based pressure sensor for human motions detection. Adv. Funct. Mater. **28**, 1802576 (2018). https://doi.org/10.1002/adfm.201802576
11. Y.H. Jung, T.X. Pham, D. Issa, H.S. Wang, J.H. Lee et al., Deep learning-based noise robust flexible piezoelectric acoustic sensors for speech processing. Nano Energy **101**, 107610 (2022). https://doi.org/10.1016/j.nanoen.2022.107610
12. Y. Wei, Y. Qiao, G. Jiang, Y. Wang, F. Wang et al., A wearable skinlike ultra-sensitive artificial graphene throat. ACS Nano **13**, 8639–8647 (2019). https://doi.org/10.1021/acsnano.9b03218
13. S. Xu, J.-X. Yu, H. Guo, S. Tian, Y. Long et al., Force-induced ion generation in zwitterionic hydrogels for a sensitive silent-speech sensor. Nat. Commun. **14**, 219 (2023). https://doi.org/10.1038/s41467-023-35893-7

14. S. Maiti, S. Kumar Karan, J. Lee, A. Kumar Mishra, B. Bhusan Khatua et al., Bio-waste onion skin as an innovative nature-driven piezoelectric material with high energy conversion efficiency. Nano Energy **42**, 282–293 (2017). https://doi.org/10.1016/j.nanoen.2017.10.041
15. S. Min, D.H. Kim, D.J. Joe, B.W. Kim, Y.H. Jung et al., Clinical validation of a wearable piezoelectric blood-pressure sensor for continuous health monitoring. Adv. Mater. **35**, e2301627 (2023). https://doi.org/10.1002/adma.202301627
16. J.H. Lee, K.H. Cho, K. Cho, Emerging trends in soft electronics: integrating machine intelligence with soft acoustic/vibration sensors. Adv. Mater. **35**, e2209673 (2023). https://doi.org/10.1002/adma.202209673
17. S. Qiu, H. Zhao, N. Jiang, Z. Wang, L. Liu et al., Multi-sensor information fusion based on machine learning for real applications in human activity recognition: state-of-the-art and research challenges. Inf. Fusion **80**, 241–265 (2022). https://doi.org/10.1016/j.inffus.2021.11.006
18. K. Zhou, C. Zhang, Z. Xiong, H.-Y. Chen, T. Li et al., Template-directed growth of hierarchical MOF hybrid arrays for tactile sensor. Adv. Funct. Mater. **30**, 2001296 (2020). https://doi.org/10.1002/adfm.202001296
19. S. Xu, A. Jayaraman, J.A. Rogers, Skin sensors are the future of health care. Nature **571**, 319–321 (2019). https://doi.org/10.1038/d41586-019-02143-0
20. Q. Zeng, F. Wang, R. Hu, X. Ding, Y. Lu et al., Debonding-on-demand polymeric wound patches for minimal adhesion and clinical communication. Adv. Sci. **9**, e2202635 (2022). https://doi.org/10.1002/advs.202202635
21. C. Liang, C. Jiao, H. Gou, H. Luo, Y. Diao et al., Facile construction of electrochemical and self-powered wearable pressure sensors based on metallic corrosion effects. Nano Energy **104**, 107954 (2022). https://doi.org/10.1016/j.nanoen.2022.107954
22. H. Yoo, E. Kim, J.W. Chung, H. Cho, S. Jeong et al., Silent speech recognition with strain sensors and deep learning analysis of directional facial muscle movement. ACS Appl. Mater. Interfaces **14**, 54157 (2022). https://doi.org/10.1021/acsami.2c14918
23. Q. Zeng, Q. Peng, F. Wang, G. Shi, H. Haick et al., Tailoring food biopolymers into biogels for regenerative wound healing and versatile skin bioelectronics. Nano-Micro Lett. **15**, 153 (2023). https://doi.org/10.1007/s40820-023-01099-1
24. E.S. Muckley, M. Naguib, H.-W. Wang, L. Vlcek, N.C. Osti et al., Multimodality of structural, electrical, and gravimetric responses of intercalated MXenes to water. ACS Nano **11**, 11118–11126 (2017). https://doi.org/10.1021/acsnano.7b05264
25. R. Yang, X. Gui, L. Yao, Q. Hu, L. Yang et al., Ultrathin, lightweight, and flexible CNT buckypaper enhanced using MXenes for electromagnetic interference shielding. Nano-Micro Lett. **13**, 66 (2021). https://doi.org/10.1007/s40820-021-00597-4
26. E. Mostafavi, S. Iravani, MXene-graphene composites: a perspective on biomedical potentials. Nano-Micro Lett. **14**, 130 (2022). https://doi.org/10.1007/s40820-022-00880-y
27. M. Hilal, W. Yang, Y. Hwang, W. Xie, Tailoring MXene thickness and functionalization for enhanced room-temperature trace NO_2 sensing. Nano-Micro Lett. **16**, 84 (2024). https://doi.org/10.1007/s40820-023-01316-x
28. W. Li, C. Teng, Y. Sun, L. Cai, J.-L. Xu et al., Sprayed, scalable, wearable, and portable NO_2 sensor array using fully flexible AgNPs-all-carbon nanostructures. ACS Appl. Mater. Interfaces **10**, 34485–34493 (2018). https://doi.org/10.1021/acsami.8b11254
29. H. Ma, M. Fashandi, Z.B. Rejeb, X. Ming, Y. Liu et al., Efficient electromagnetic wave absorption and thermal infrared stealth in PVTMS@MWCNT nano-aerogel *via* abundant nano-sized cavities and attenuation interfaces. Nano-Micro Lett. **16**, 20 (2023). https://doi.org/10.1007/s40820-023-01218-y
30. F.-L. Gao, J. Liu, X.-P. Li, Q. Ma, T. Zhang et al., $Ti_3C_2T_x$ MXene-based multifunctional tactile sensors for precisely detecting and distinguishing temperature and pressure stimuli. ACS Nano **17**, 16036–16047 (2023). https://doi.org/10.1021/acsnano.3c04650
31. Y. Yu, P. Yi, W. Xu, X. Sun, G. Deng et al., Environmentally tough and stretchable MXene organohydrogel with exceptionally enhanced electromagnetic interference shielding performances. Nano-Micro Lett. **14**, 77 (2022). https://doi.org/10.1007/s40820-022-00819-3
32. H.F. Lei, Z.Q. Zhang, B. Liu, Effect of fiber arrangement on mechanical properties of short fiber reinforced composites. Compos. Sci. Technol. **72**, 506–514 (2012). https://doi.org/10.1016/j.compscitech.2011.12.011
33. A. Godara, L. Mezzo, F. Luizi, A. Warrier, S.V. Lomov et al., Influence of carbon nanotube reinforcement on the processing and the mechanical behaviour of carbon fiber/epoxy composites. Carbon **47**, 2914–2923 (2009). https://doi.org/10.1016/j.carbon.2009.06.039
34. Q. Zeng, X. Qi, G. Shi, M. Zhang, H. Haick, Wound dressing: from nanomaterials to diagnostic dressings and healing evaluations. ACS Nano **16**, 1708–1733 (2022). https://doi.org/10.1021/acsnano.1c08411
35. Q. Zeng, Y. Qian, Y. Huang, F. Ding, X. Qi et al., Polydopamine nanoparticle-dotted food gum hydrogel with excellent antibacterial activity and rapid shape adaptability for accelerated bacteria-infected wound healing. Bioact. Mater. **6**, 2647–2657 (2021). https://doi.org/10.1016/j.bioactmat.2021.01.035
36. A. Sarycheva, Y. Gogotsi, Raman spectroscopy analysis of the structure and surface chemistry of $Ti_3C_2T_x$ MXene. MXenes. Jenny Stanford Publishing, (2023), pp 333–355 https://doi.org/10.1201/9781003306511-16
37. S.-N. Li, Z.-R. Yu, B.-F. Guo, K.-Y. Guo, Y. Li et al., Environmentally stable, mechanically flexible, self-adhesive, and electrically conductive $Ti_3C_2T_X$ MXene hydrogels for wide-temperature strain sensing. Nano Energy **90**, 106502 (2021). https://doi.org/10.1016/j.nanoen.2021.106502
38. C. Branca, G. D'Angelo, C. Crupi, K. Khouzami, S. Rifici et al., Role of the OH and NH vibrational groups in polysaccharide-nanocomposite interactions: a FTIR-ATR

study on chitosan and chitosan/clay films. Polymer **99**, 614–622 (2016). https://doi.org/10.1016/j.polymer.2016.07.086

39. V. Natu, M. Benchakar, C. Canaff, A. Habrioux, S. Célérier et al., A critical analysis of the X-ray photoelectron spectra of $Ti_3C_2T_z$ MXenes. Matter **4**, 1224–1251 (2021). https://doi.org/10.1016/j.matt.2021.01.015
40. J. Ren, Z. Wang, P. Xu, C. Wang, F. Gao et al., Porous Co_2VO_4 nanodisk as a high-energy and fast-charging anode for lithium-ion batteries. Nano-Micro Lett. **14**, 5 (2021). https://doi.org/10.1007/s40820-021-00758-5
41. K. Zou, P. Cai, B. Wang, C. Liu, J. Li et al., Insights into enhanced capacitive behavior of carbon cathode for lithium ion capacitors: the coupling of pore size and graphitization engineering. Nano-Micro Lett. **12**, 121 (2020). https://doi.org/10.1007/s40820-020-00458-6
42. Y. Qin, M. Long, B. Tan, B. Zhou, RhB adsorption performance of magnetic adsorbent Fe_3O_4/RGO composite and its regeneration through A Fenton-like reaction. Nano-Micro Lett. **6**, 125–135 (2014). https://doi.org/10.1007/BF03353776
43. L. Zhao, H. Li, J. Meng, A.C. Wang, P. Tan et al., Reversible conversion between Schottky and ohmic contacts for highly sensitive, multifunctional biosensors. Adv. Funct. Mater. **30**, 1907999 (2020). https://doi.org/10.1002/adfm.201907999
44. H. Zhi, X. Zhang, F. Wang, P. Wan, L. Feng, Flexible $Ti_3C_2T_x$ MXene/PANI/bacterial cellulose aerogel for e-skins and gas sensing. ACS Appl. Mater. Interfaces **13**, 45987 (2021). https://doi.org/10.1021/acsami.1c12991
45. X. Wu, Z. Li, Y. Zhu, J. Wang, S. Yang, Ultralight GO-hybridized CNTs aerogels with enhanced electronic and mechanical properties for piezoresistive sensors. ACS Appl. Mater. Interfaces **13**, 26352–26361 (2021). https://doi.org/10.1021/acsami.1c04080
46. Y. Ma, Y. Yue, H. Zhang, F. Cheng, W. Zhao et al., 3D synergistical MXene/reduced graphene oxide aerogel for a piezoresistive sensor. ACS Nano **12**, 3209–3216 (2018). https://doi.org/10.1021/acsnano.7b06909
47. R. Liu, J. Li, M. Li, Q. Zhang, G. Shi et al., MXene-coated air-permeable pressure-sensing fabric for smart wear. ACS Appl. Mater. Interfaces **12**, 46446 (2020). https://doi.org/10.1021/acsami.0c11715
48. Q. Yu, C. Su, S. Bi, Y. Huang, J. Li et al., $Ti_3C_2T_x$@nonwoven fabric composite: promising MXene-coated fabric for wearable piezoresistive pressure sensors. ACS Appl. Mater. Interfaces **14**, 9632 (2022). https://doi.org/10.1021/acsami.2c00980
49. W. Shi, S. Chen, Y. Lin, G. Zhang, Z. Peng et al., Piezoresistive fibers with record high sensitivity *via* the synergic optimization of porous microstructure and elastic modulus. Chem. Eng. J. **441**, 136046 (2022). https://doi.org/10.1016/j.cej.2022.136046
50. W. Du, Z. Li, Y. Zhao, X. Zhang, L. Pang et al., Biocompatible and breathable all-fiber-based piezoresistive sensor with high sensitivity for human physiological movements monitoring. Chem. Eng. J. **446**, 137268 (2022). https://doi.org/10.1016/j.cej.2022.137268
51. J. Huang, D. Li, M. Zhao, H. Ke, A. Mensah et al., Flexible electrically conductive biomass-based aerogels for piezoresistive pressure/strain sensors. Chem. Eng. J. **373**, 1357–1366 (2019). https://doi.org/10.1016/j.cej.2019.05.136
52. D.-J. Yao, Z. Tang, L. Zhang, Z.-G. Liu, Q.-J. Sun et al., A highly sensitive, foldable and wearable pressure sensor based on MXene-coated airlaid paper for electronic skin. J. Mater. Chem. C **9**, 12642–12649 (2021). https://doi.org/10.1039/D1TC02458B
53. S. Wang, W. Deng, T. Yang, Y. Ao, H. Zhang et al., Bioinspired MXene-based piezoresistive sensor with two-stage enhancement for motion capture. Adv. Funct. Mater. **33**, 2214503 (2023). https://doi.org/10.1002/adfm.202214503
54. X. Cao, J. Zhang, S. Chen, R.J. Varley, K. Pan, 1D/2D nanomaterials synergistic, compressible, and response rapidly 3D graphene aerogel for piezoresistive sensor. Adv. Funct. Mater. **30**, 2003618 (2020). https://doi.org/10.1002/adfm.202003618
55. D. Liao, Y. Wang, P. Xie, C. Zhang, M. Li et al., A resilient and lightweight cellulose/graphene oxide/polymer-derived multifunctional carbon aerogel generated from Pickering emulsion toward a wearable pressure sensor. J. Colloid Interface Sci. **628**, 574–587 (2022). https://doi.org/10.1016/j.jcis.2022.07.188
56. L. Li, X. Fu, S. Chen, S. Uzun, A.S. Levitt et al., Hydrophobic and stable MXene-polymer pressure sensors for wearable electronics. ACS Appl. Mater. Interfaces **12**, 15362 (2020). https://doi.org/10.1021/acsami.0c00255
57. Z. Yang, H. Li, S. Zhang, X. Lai, X. Zeng, Superhydrophobic MXene@carboxylated carbon nanotubes/carboxymethyl chitosan aerogel for piezoresistive pressure sensor. Chem. Eng. J. **425**, 130462 (2021). https://doi.org/10.1016/j.cej.2021.130462
58. X. Chen, H. Liu, Y. Zheng, Y. Zhai, X. Liu et al., Highly compressible and robust polyimide/carbon nanotube composite aerogel for high-performance wearable pressure sensor. ACS Appl. Mater. Interfaces **11**, 42594 (2019). https://doi.org/10.1021/acsami.9b14688
59. L. Wang, M. Zhang, B. Yang, J. Tan, X. Ding, Highly compressible, thermally stable, light-weight, and robust aramid nanofibers/Ti_3AlC_2 MXene composite aerogel for sensitive pressure sensor. ACS Nano **14**, 10633–10647 (2020). https://doi.org/10.1021/acsnano.0c04888
60. X. Shi, X. Fan, Y. Zhu, Y. Liu, P. Wu et al., Pushing detectability and sensitivity for subtle force to new limits with shrinkable nanochannel structured aerogel. Nat. Commun. **13**, 1119 (2022). https://doi.org/10.1038/s41467-022-28760-4
61. S. Han, Q. Wu, J. Zhu, J. Zhang, A. Chen et al., Multifunctional, superelastic, and environmentally stable sodium alginate/mxene/polydimethylsiloxane aerogels for piezoresistive sensor. Chem. Eng. J. **471**, 144551 (2023). https://doi.org/10.1016/j.cej.2023.144551
62. Z. Deng, C. Gao, S. Feng, H. Zhang, Y. Liu et al., Highly compressible, light-weight and robust nitrogen-doped graphene composite aerogel for sensitive pressure sensors. Chem. Eng. J. **471**, 144790 (2023). https://doi.org/10.1016/j.cej.2023.144790

63. Y. Hu, H. Zhuo, Q. Luo, Y. Wu, R. Wen et al., Biomass polymer-assisted fabrication of aerogels from MXenes with ultrahigh compression elasticity and pressure sensitivity. J. Mater. Chem. A **7**, 10273–10281 (2019). https://doi.org/10.1039/C9TA01448A
64. Z. Qin, Y. Lv, X. Fang, B. Zhao, F. Niu et al., Ultralight polypyrrole crosslinked nanofiber aerogel for highly sensitive piezoresistive sensor. Chem. Eng. J. **427**, 131650 (2022). https://doi.org/10.1016/j.cej.2021.131650
65. Z. Chen, H. Zhuo, Y. Hu, H. Lai, L. Liu et al., Wood-derived lightweight and elastic carbon aerogel for pressure sensing and energy storage. Adv. Funct. Mater. **30**, 1910292 (2020). https://doi.org/10.1002/adfm.201910292
66. J. Zhou, Y.-L. Hsieh, Conductive polymer protonated nanocellulose aerogels for tunable and linearly responsive strain sensors. ACS Appl. Mater. Interfaces **10**, 27902–27910 (2018). https://doi.org/10.1021/acsami.8b10239
67. S. Long, Y. Feng, F. He, S. He, H. Hong et al., An ultralight, supercompressible, superhydrophobic and multifunctional carbon aerogel with a specially designed structure. Carbon **158**, 137–145 (2020). https://doi.org/10.1016/j.carbon.2019.11.065
68. M. Xie, G. Qian, Y. Yu, C. Chen, H. Li et al., High-performance flexible reduced graphene oxide/polyimide nanocomposite aerogels fabricated by double crosslinking strategy for piezoresistive sensor application. Chem. Eng. J. **480**, 148203 (2024). https://doi.org/10.1016/j.cej.2023.148203
69. W. Jiang, C. Yao, W. Chen, D. Li, L. Zhong et al., A super-resilient and highly sensitive graphene oxide/cellulose-derived carbon aerogel. J. Mater. Chem. A **8**, 18376–18384 (2020). https://doi.org/10.1039/D0TA05310D
70. W. Ma, Z. Jiang, T. Lu, R. Xiong, C. Huang, Lightweight, elastic and superhydrophobic multifunctional nanofibrous aerogel for self-cleaning, oil/water separation and pressure sensing. Chem. Eng. J. **430**, 132989 (2022). https://doi.org/10.1016/j.cej.2021.132989
71. Z. Wang, Y. Wang, Y. Chen, M. Yousaf, H. Wu et al., Reticulate dual-nanowire aerogel for multifunctional applications: a high-performance strain sensor and a high areal capacity rechargeable anode. Adv. Funct. Mater. **29**, 1807467 (2019). https://doi.org/10.1002/adfm.201807467
72. T. Xu, Q. Song, K. Liu, H. Liu, J. Pan et al., Nanocellulose-assisted construction of multifunctional MXene-based aerogels with engineering biomimetic texture for pressure sensor and compressible electrode. Nano-Micro Lett. **15**, 98 (2023). https://doi.org/10.1007/s40820-023-01073-x
73. M. Touron, C. Celle, L. Orgéas, J.-P. Simonato, Hybrid silver nanowire-CMC aerogels: from 1D nanomaterials to 3D electrically conductive and mechanically resistant lightweight architectures. ACS Nano **16**, 14188–14197 (2022). https://doi.org/10.1021/acsnano.2c04288
74. D. Yang, X. Dong, L. Jiang, F. Liu, S. Ma et al., A universal biomacromolecule-enabled assembly strategy for constructing multifunctional aerogels with 90% inorganic mass loading from inert nano-building blocks. Small **20**, e2402334 (2024). https://doi.org/10.1002/smll.202402334
75. H. Wang, Y. Jiang, Z. Ma, Y. Shi, Y. Zhu et al., Hyperelastic, robust, fire-safe multifunctional MXene aerogels with unprecedented electromagnetic interference shielding efficiency. Adv. Funct. Mater. **33**, 2306884 (2023). https://doi.org/10.1002/adfm.202306884
76. L. Zhuang, D. Lu, J. Zhang, P. Guo, L. Su et al., Highly cross-linked carbon tube aerogels with enhanced elasticity and fatigue resistance. Nat. Commun. **14**, 3178 (2023). https://doi.org/10.1038/s41467-023-38664-6
77. J. Xu, H. Chang, B. Zhao, R. Li, T. Cui et al., Highly stretchable and conformal electromagnetic interference shielding armor with strain sensing ability. Chem. Eng. J. **431**, 133908 (2022). https://doi.org/10.1016/j.cej.2021.133908